Internal Displacement and Strain Imaging Using Ultrasonic Speckle Tracking

Matthew O'Donnell, *Fellow, IEEE*, Andrei R. Skovoroda,
Benjamin M. Shapo, and Stanislav Y. Emelianov, *Member, IEEE*

Abstract—Previous ultrasound speckle tracking methods have been extended, permitting measurement of internal displacement and strain fields over a wide dynamic range of tissue motion. The markedly increased dynamic range of this approach should lead to enhanced contrast resolution in strain and elasticity images. Results of experiments on gelatin-based, tissue equivalent phantoms show the capabilities of the method.

I. INTRODUCTION

FOR MANY years, palpation was the primary screening technique to detect many cancers. Today, in spite of numerous new imaging modalities, palpation is still widely used as a self-screening procedure for hard masses in the breast and testes. Its efficacy, however, is limited to abnormalities located relatively close to the skin surface. Recently, a number of investigators have proposed elasticity imaging as a new diagnostic method for many pathologies, including breast cancers [1]–[16]. The goal of elasticity imaging is to develop surrogate, remote palpation, thus expanding its limited range to include deep lying lesions. Such imaging may permit differential diagnosis based on significant variation in the Young's modulus of elasticity. However, no convenient imaging modalities, including ultrasound, nuclear magnetic resonance and computed tomography, can directly provide information about this fundamental tissue parameter.

One approach to elasticity imaging is to reconstruct the mechanical properties of tissue based on measurement of internal deformations under the action of applied external forces. Using real-time ultrasound, tissue motion can be measured with speckle tracking algorithms, followed by computation of internal strains and complete reconstruction of the elasticity distribution. Quantitative elasticity imaging, therefore, consists of three main components: speckle tracking and evaluation of tissue motion, estimation of strain tensor components, and reconstruction of the elastic modulus based on strain images. In this report, we focus on the steps of speckle tracking and quantitative estimation of internal strains. In a companion paper, we compare the experimental results presented below

to the predictions of a linear elastic model, as well as discuss several aspects of elastic modulus reconstruction [17].

Many speckle tracking routines have been proposed, notably the recent work of Trahey *et al* on angle independent flow imaging [18]. This 2-D tracking procedure generalizes a correlation search method first proposed for removing phase aliases in pulsed Doppler measurements [19]. Correlation based processing has also been used to estimate tissue motion in a number of studies [3]–[7], [12], [16], [20], [21]. In contrast, a number of other studies employed traditional Doppler and color flow imaging methods to detect tissue motion [1], [2], [9], [10], [13], [15]. These competing approaches have advantages and deficiencies, where the primary benefit of the direct correlation method is that axial motion exceeding a quarter of an ultrasonic wavelength (i.e., $\lambda/4$) can be tracked without ambiguity. Recently, we proposed a Fourier based speckle tracking procedure for 2-D motion estimation [22]. A subset of this processing closely parallels Doppler methods for measuring axial motion. Fundamental differences between this method and traditional correlation based approaches for tracking axial motion are discussed in Section II.

Two groups have independently proposed measurement of internal strains to evaluate tissue elasticity [8], [11], [12], [15], [16]. Using a simple linear model, Ophir *et al.* have shown that the Young's modulus can be directly computed from quantitative strain measurements [12]. More detailed 2- and 3-D analysis by Sarvazyan and Skovoroda has shown that, even though this simple dependence does not generally hold, there is a very strong link between intrinsic elastic constants and the strain tensor [8], [11]. Thus, there is strong motivation to accurately estimate both internal strain and displacement. Since estimation errors for uniform motion of a speckle generating object are determined primarily by the signal to noise ratio, bandwidth and carrier frequency of the ultrasound system, as discussed in Section II, it would appear that large internal displacements are desired to maximize the signal to noise ratio of displacement and strain estimates. Unfortunately, all speckle tracking methods fail in the limit of large displacements and strains even in the linear elastic regime due to significant changes in the spatial distribution of scatterers used for tracking. Large displacements can move scatterers in and out of the plane of the imaging system. Large strains change the spatial distribution of scatterers within an area of an image, thus decorrelating the speckle patterns used for motion tracking. Substantial decorrelation of speckle

markedly increases errors in displacement and strains derived from the displacement.

To demonstrate how finite strains can limit the accuracy of motion estimates, we use a simple one-dimensional (1-D) simulation of ultrasound speckle in the presence of strain. This model assumes an ultrasound transducer with a Gaussian impulse response centered at 5 MHz. This pulse is convolved with a collection of equal amplitude reflectors randomly positioned along a line with a mean separation between scatterers of about 2.5 μm (i.e., about 50 scatterers per wavelength at the carrier frequency). This distribution produces fully developed speckle in the RF *A*-Scan (i.e., circular Gaussian statistics with Rayleigh amplitude and uniform phase probability density functions). Variable magnitude Gaussian distributed noise with bandwidth matched to the transducer bandwidth is added to this idealized waveform. The noise magnitude is specified by the signal to noise ratio (SNR), computed as the ratio of the power in the idealized signal to the power in the additive noise integrated over the segment of the waveform used for correlation analysis. A second idealized RF *A*-Scan is produced by displacing the scatterers, where the magnitude of the displacement is a linear function of range (i.e., constant strain). An independent noise signal satisfying the same statistics as the first signal is then added to this waveform.

Segments from a typical set of waveforms sampled at 160 MHz for a 40% fractional bandwidth are presented in Fig. 1. The solid line represents the RF *A*-Scan prior to displacement and the dashed line is the RF *A*-Scan after displacement by

$$\Delta R(R) = [\Delta R]_0 - 0.05R, \qquad (1)$$

where R is the range of the scatterer and $[\Delta R]_0$ is the displacement of a scatterer at zero range. Note that (1) represents an equivalent internal strain magnitude of 5%. The signal is displaced by about half a period of the carrier frequency at the center of the *A*-Scan in Fig. 1. Comparison of the dashed and solid signals shows that the displacement is more than half a cycle near the front and less than half a cycle near the end. Consequently, these signals are highly decorrelated.

Errors in strain estimates resulting from the decorrelation evident in Fig. 1 can be assessed with the same simulation. The strain is computed using the RF correlation method of [12], which includes quadratic interpolation as described in [23] and [24]. The correlation is computed over a 4 μs integration period (i.e., window), where the signal to noise ratio of the RF waveform is assumed to be about 30 dB. For these conditions, errors in displacement estimates for very small values of the strain are small but nonzero. The standard deviation in the strain is plotted as a function of the strain in Fig. 2. It is computed by performing multiple correlation measurements for the same displacement function, where each measurement uses a different scatterer distribution and noise signal. Clearly, the error is not a linear function of the strain. At small strains the error is determined primarily by the details of the ultrasound system (i.e., SNR, bandwidth, duration of correlation window). At large strains, speckle decorrelation produces substantial errors.
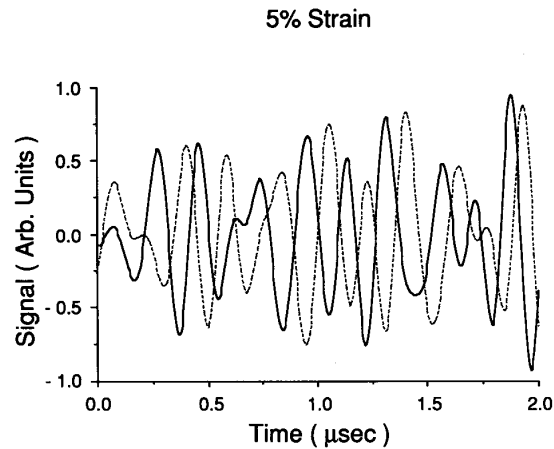
5% Strain

Fig. 1.   One-dimensional simulation results of speckle signals in the presence of significant (5%) internal strain. Solid line represents original RF *A*-Scan, and dashed line is the RF *A*-Scan after application of 5% internal strain.
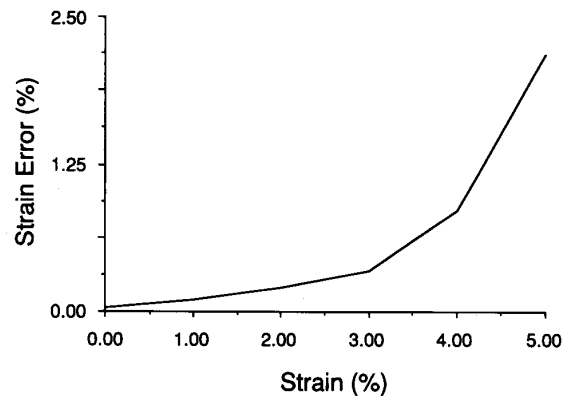

Fig. 2.   Strain error (standard deviation of the strain) as a function of the internal strain estimated from the 1-D simulation at a fixed correlation integration time.

One possible strategy to decrease decorrelation effects is to shorten the correlation window. This reduces error at large strain values but should increase relative error at small strain values since the signal to noise ratio is reduced. In Fig. 3 the strain signal to noise ratio, defined as the ratio of the strain to the strain standard deviation, is plotted as a function of strain for two different correlation integration times. The solid curve (reduced integration time) is computed using twice the number of points since there are twice as many independent displacement estimates. As expected, at high strain values the relative strain error decreases with reduced integration time. At low strains where speckle decorrelation is less of a problem, the longer integration time yields better results.

Although this 1-D simulation represents a gross simplification of strain measurements made with an actual ultrasound imaging system, results presented in Figs. 1–3 clearly define the problem in obtaining sensitive strain measurements. Large internal displacements are desired since errors in displacement estimates for uniform motion are relatively insensitive to the absolute magnitude of the displacement. However, significant
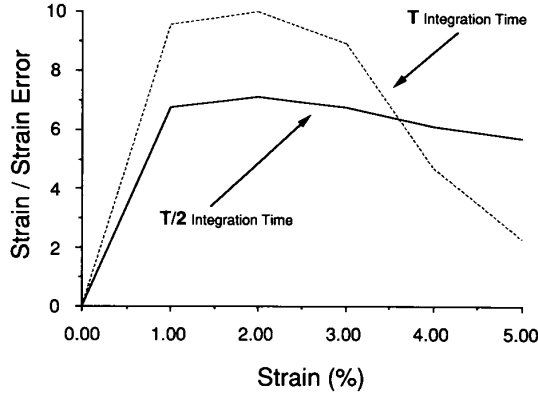
Fig. 3. Strain signal to noise ratio as a function of internal strain estimated from the 1-D simulation for two different correlation integration times.

strains associated with large internal displacements in a constrained body result in substantial errors in both displacement and strain estimates. It is the fundamental hypothesis of this paper that this restriction can be greatly reduced allowing accurate displacement and strain estimates for large internal displacements and strains. The details of this method, representing an extension of the speckle tracking approach discussed in Section II, are presented in Section III.

Finally, measurements on tissue equivalent phantoms have been performed to test both the displacement and strain imaging ideas of Sections II and III. These experiments are summarized in Section IV. The paper concludes in Section V with a discussion of the results.

II. SPECKLE TRACKING ALGORITHM

As described in [3]–[7], [12], [16], [18]–[21], uniform motion of a speckle generating object can be analyzed using correlation processing. In this study, we only consider motion of an object along the direction of beam propagation (i.e., axial motion). Motion orthogonal to the beam direction, or cross-beam motion, is not considered here but is discussed in Section V. For an isolated point scatterer lying along the beam line, the RF signal recorded by an ultrasound imaging system can be modelled as

$$x_1(t) = S(t - \tau_1) = A(t - \tau_1)\cos[\omega_0(t - \tau_1)], \quad (2)$$

where ω_0 is the angular frequency of the ultrasound carrier, τ_1 is the round-trip propagation time from the transducer to the point scatterer, S is the impulse response, and A the real envelope of the transceived pulse. On a subsequent measurement, where the object moves axially between recordings due to an externally applied force, the signal becomes:

$$x_2(t) = S(t - \tau_2) = A(t - \tau_2)\cos[\omega_0(t - \tau_2)]. \quad (3)$$

The axial displacement of the particle is simply related to the difference in time delays, $\Delta R = c(\tau_2 - \tau_1)/2 = c\tau_{RF}/2$, where c is the sound velocity. Consequently, the displacement between measurements can be obtained from the peak position of the cross correlation function between $x_1(t)$ and $x_2(t)$

computed over integration time T,

$$C(t) = \frac{1}{T} \int_0^T x_1(\tau)x_2(t + \tau)d\tau, \quad (4)$$

where MAX $(C(t)) = C(\tau_{RF})$. For a sampled system, the integral of (4) is replaced by a discrete sum, and the peak position is found with an interpolation algorithm, such as the one described in [23], [24]. Although presented for an isolated scatterer, the correlation method embodied in (4) can be used to track more complex scattering distributions such as speckle.

If the integration period T of the correlation analysis is long compared to the impulse response of the system (i.e., long compared to the duration of the envelope function $A(t)$) and the signal to noise ratio of the RF waveform is significantly above 1, then the variance in the shift estimate is [24]–[27]:

$$[\sigma_\tau^2]_{RF} = 2\left[\frac{\Gamma_{nn}(0)}{\omega_0^2\Gamma_{SS}(0)}\right]\left[1 + \frac{(\Delta\omega)^2}{(\omega_0)^2}\right]^{-1},$$

$$= \left[\frac{2}{\omega_0^2 \text{ SNR}}\right]\left[1 + \frac{(\Delta\omega)^2}{(\omega_0)^2}\right]^{-1}. \quad (5)$$

In (5), the ratio of $\Delta\omega$ to ω_0 represents the fractional bandwidth of the imaging system. The function $\Gamma_{nn}(0)$ is the autocorrelation of the additive noise evaluated at zero lag, which equals the noise power integrated over the correlation interval. Similarly, $\Gamma_{SS}(0)$ is the autocorrelation function of the signal at zero lag, which equals the signal power integrated over the correlation interval. The SNR in (5), therefore, represents the power signal to noise ratio integrated over the correlation interval, as discussed in Section I. For fully developed speckle, the SNR is simply proportional to the integration time T. Finally, we note that the variance is **not** simply proportional to the inverse square of the bandwidth $\Delta\omega$, as is often stated [24], [26].

In contrast to computationally intensive RF methods, the correlation function between two time signals can be performed using base-band analysis. The base-band representations of the two signals $x_1(t)$ and $x_2(t)$ are:

$$\tilde{x}_1(t) = A(t - \tau_1)e^{-i\omega_0\tau_1},$$

$$\tilde{x}_2(t) = A(t - \tau_2)e^{-i\omega_0\tau_2}. \quad (6)$$

As described in [28], the complex correlation function between these two signals can be evaluated according to the expression

$$\tilde{C}(t) = \frac{1}{T}\int_0^T \tilde{x}_1(\tau)\tilde{x}_2^*(t + \tau)d\tau. \quad (7)$$

At zero lag, the complex correlation reduces to

$$\tilde{C}(0) = \Gamma_{AA}(\tau)e^{-i\omega_0\tau}, \quad (8)$$

where $\Gamma_{AA}(\tau)$ is the autocorrelation function of the envelope evaluated at time τ. The time shift between $x_1(t)$ and $x_2(t)$ can therefore be estimated from the phase of the zero lag complex correlation function, i.e.,

$$\tau_{BB} = \frac{\phi(0)}{\omega_0} = \frac{\tan^{-1}\left[\frac{\text{Im}(\tilde{C}(0))}{\text{Re}(\tilde{C}(0))}\right]}{\omega_0}. \quad (9)$$

Note again that in a sampled system the integral of (7) is approximated by a discrete sum.

Assuming that the integration time T is large compared to the duration of the envelope, a simple propagation of error analysis yields the following expression for the variance of the time shift estimated from the phase of the zero lag complex correlation function

$$[\sigma_\tau^2]_{\text{BB}} = 2\left[\frac{\Gamma_{nn}(0)}{\omega_0^2 \Gamma_{AA}(\tau)}\right],$$

$$= \left[\frac{2}{\omega_0^2 \text{ SNR}}\right]\left[\frac{\Gamma_{AA}(0)}{\Gamma_{AA}(\tau)}\right]. \tag{10}$$

This expression is very similar to the variance for the full RF correlation search, where the ratio between the variances for base-band versus RF estimation is:

$$\frac{[\sigma_\tau^2]_{\text{BB}}}{[\sigma_\tau^2]_{\text{RF}}} = \left[\frac{\Gamma_{AA}(0)}{\Gamma_{AA}(\tau)}\right]\left[1 + \frac{(\Delta\omega)^2}{(\omega_0)^2}\right]. \tag{11}$$

As is evident from (11), the variance in estimates of the time shift obtained from simple baseband processing closely approximates that of full RF processing. For example, given a imaging system with a fractional bandwidth of 40% and a shift between 0 and 0.5 times the period of the carrier, the ratio of the standard deviations of baseband to RF estimates varies between only 1.08 and 1.18. Extensive simulations using the 1-D model discussed in Section I have confirmed this relation provided that the product of the correlation period and the bandwidth ($\Delta\omega T$) is greater than 4π. For very low SNR's, complex baseband processing is actually more robust because it avoids the peak hopping ambiguity discussed in [25]. A set of 1-D simulations was conducted to test this hypothesis, as well as to test the general validity of (5) and (10). A specific example from this set illustrates the similarity of the two methods.

Assuming a 40% fractional bandwidth, 5 MHz Gaussian pulse, an RF A-Scan was produced by convolution with the 1-D scatterer distribution described in Section I. Gaussian noise matched in bandwidth to this pulse was added to the signal. A second RF A-Scan was produced by uniformly delaying the original scatterer distribution by 20 ns and adding an independent snapshot of the same Gaussian noise source to the ideal waveform. Both RF and base-band correlation analyses were performed on these signals over a integration time of 4 μs. The analysis was repeated 100 times, where independent scatterer distributions and noise snapshots were used for each trial. According to (5) and (10), the standard deviation in the time shift estimate should be about 15 ns for both RF and baseband processing assuming a 10 dB SNR. The actual standard deviations were 32.8 ns for RF processing and 15.4 ns for baseband processing. The large standard deviation for RF processing was the direct result of 5 cases where the correlation search routine hopped by at least one full period of the carrier. Removal of these trials reduced the RF standard deviation to 14.6 ns, a value nearly equal to the baseband result.

The error analysis presented above indicates that simple baseband processing can measure displacements with accuracy

equivalent to full RF correlation analysis for shifts small compared to the duration of the envelope of the ultrasound signal and less than half the period of the carrier frequency. If shifts greater than half the period of the carrier frequency occur, then aliasing will result. In the remainder of this section, the application of baseband processing to displacement estimation for motion less than $\lambda/4$ at the carrier frequency is discussed.

For displacement imaging, a complex baseband signal $\widetilde{x_{nm}^1}$, often referred to as a base-band image, is generated at each pixel (n, m) in the image plane prior to deformation. A second baseband image $\widetilde{x_{nm}^2}$ is recorded following deformation. To minimize errors for either axial or lateral displacements comparable to $\lambda/4$, initial baseband images $\widetilde{x_{nm}^1}$ and $\widetilde{x_{nm}^2}$ must be spatially low-pass filtered so that the resultant effective 2-D envelope function (i.e., 2-D speckle spot size) is much larger than any relevant displacement. That is, two new images are generated of the form

$$\widetilde{y_{nm}^1} = \text{LPF}\left[\widetilde{x_{nm}^1}\right],$$

$$\widetilde{y_{nm}^2} = \text{LPF}\left[\widetilde{x_{nm}^2}\right]. \tag{12}$$

We have used two forms of low pass filtering. First, the bandwidth of the system is reduced so that the extent of the signal envelope A is significantly larger than any displacement. Although elongating the envelope, this processing does not reduce the variance in image magnitude due to speckle noise. And second, a simple 2-D moving average filter is applied to the resultant narrow-band image. This spatial low pass filtering increases the size of a coherent speckle spot, and thus reduces large scale fluctuations in the magnitude of $|\tilde{y}|$ due to nonaxial motion.

After filtering, the complex conjugate product of the images is computed for subsequent correlation analysis,

$$\widetilde{y_{nm}} = \left[\widetilde{y_{nm}^2}\right]\left[\widetilde{y_{nm}^1}\right]^*. \tag{13}$$

Note that each pixel of the image $\widetilde{y_{nm}}$ represents an independent term in the correlation sum (integral) at zero lag. Therefore, the zero lag complex correlation function can be evaluated at each pixel simply by low pass filtering $\widetilde{y_{nm}}$. The ultimate result of this processing is a new image, $\tilde{z}$, defined as

$$\widetilde{z_{nm}} = \text{LPF}[\widetilde{y_{nm}}], \tag{14}$$

where again a simple 2-D moving average filter is employed in this paper. The 2-D filter performs the integration of (7) as well as averaging the correlation function over the extent of the filter window. The phase of $\widetilde{z_{nm}}$ is used to estimate displacement. Note that the phase itself is **not** low pass filtered, a suboptimal process due to the nonlinear, inverse tangent function.

With phase sensitive processing, the displacement can be estimated as long its magnitude is small over the entire image plane. If the magnitude of the displacement exceeds a quarter of an ultrasonic wavelength (i.e., $\lambda/4$), then aliasing will occur in the phase measurement. Large absolute displacements are desired, however, for quantitative elasticity imaging since spatial derivatives of the displacement, i.e., strains, must be

computed. Methods for phase sensitive displacement and strain imaging for large absolute displacements are described in the next section.

III. DISPLACEMENT AND STRAIN IMAGING

Phase sensitive processing cannot unambiguously track motion greater than $\lambda/4$. This is a severe restriction on strain imaging, as discussed in Section I. To overcome this, we have developed two variations on traditional phase sensitive processing, extending its application to displacements far in excess of an ultrasonic wavelength. In addition, a method for strain estimation directly from baseband images, rather than from spatial derivatives of the estimated displacement, has been developed to reduce estimation error. The combination of these methods can produce internal strain images based on phase sensitive speckle tracking.

In Fig. 4 we illustrate the measurement geometry used to describe the basic methods for displacement and strain imaging. The mechanical body under study is placed in direct contact with an ultrasound imaging array. Immersion of the body in a water bath insures adequate coupling of the entire array to the object. The body is displaced in a controlled way at the surface by a piston, where we assume a 2-D geometry and only vertical components of the displacement are computed. Note that the piston is shown at a single vertical position, although this piston, or a set of pistons, can be positioned anywhere along the surface of the body. Before recording images, the vertical piston contacts the body, immobilizing its lowest parts against the surface of the array. This is considered the starting position for all subsequent displacement and strain measurements. By defining the initial state of the mechanical body in this way, a number of points in contact with the array do not move no matter what surface displacements are applied. These stationary points can be used for the first modification to traditional phase sensitive processing which removes phase aliases for displacements greater than $\lambda/4$.

Given that the displacement is zero at a particular point, or a particular set of points, an unwrap procedure can be developed to remove phase aliases. In general, the differential displacement between any two neighboring vertical pixels in a displacement image is

$$\Delta[u_2]_{nm} = [u_2]_{nm} - [u_2]_{nm-1}, \qquad (15)$$

where $[u_2]_{nm}$ is the vertical component of the displacement. Based on the relationship between phase and vertical displacement, (15) can be restated as

$$\Delta[u_2]_{nm} = \frac{c[\phi_{nm} - \phi_{nm-1}]}{2\omega_0}, \qquad (16)$$

where ϕ_{nm} is the phase of $\widetilde{z_{nm}}$. The differential displacement, however, can be directly computed from the processed image $\tilde{z}_{nm}$ such that (16) becomes

$$\Delta[u_2]_{nm} = \left[\frac{c}{2\omega_0}\right] \angle \left[\tilde{z}_{nm}\tilde{z}^*_{nm-1}\right], \qquad (17)$$

where $\angle \left[\tilde{z}_{nm}\tilde{z}^*_{nm-1}\right]$ represents the phase of the complex conjugate multiplication of $\tilde{z}_{nm}$ with $\tilde{z}_{nm-1}$. This expression
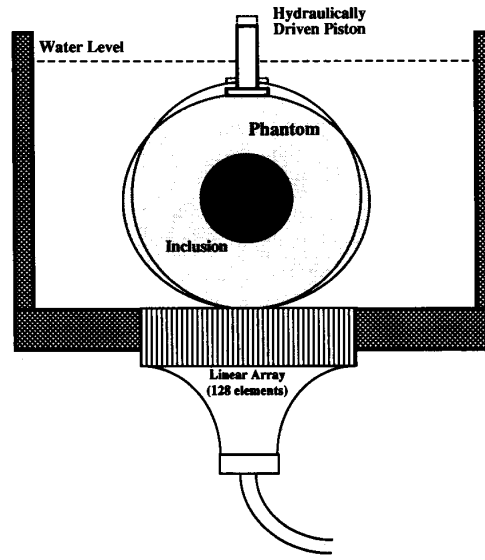

Fig. 4. Schematic of displacement and strain imaging geometry. A cylindrical phantom 88 mm in diameter and 150 mm in length was used, where a single piston vertically deformed the phantom as shown. The bottom of the phantom contacted a 128 element transducer array which imaged the phantom cross section at the central plane.

will only alias if the **differential** displacement is greater than $\lambda/4$, corresponding to a differential phase change of π. Note that, in general, $\Delta[u_2]_{nm}$ can be computed using any other pixel in the image which has similar displacement to that at (n, m). In this paper, only one of the four nearest neighbors to the pixel (n, m) is used to compute $\Delta[u_2]_{nm}$.

Assuming that the displacement field within a mechanical body is continuous, the differential displacement at any pixel is small compared to the total displacement. Therefore, phase aliases resulting from displacements greater than $\lambda/4$ can be largely removed by estimating the differential displacement everywhere in the image plane. The total displacement at every position is obtained by unwrapping (i.e., integrating) the differential displacements starting at a known position. In this study, the total vertical displacement was obtained by unwrapping differential displacements relative to the stationary point (i.e., $[u_2]_{ij}$) at the center of the transducer array. That is, the vertical displacement at any arbitrary position (n, m) relative to the stationary point at pixel (i, j) is

$$[u_2]_{nm} = [u_2]_{ij} + \sum_{k=i,l=j}^{k=n,l=m}$$

$$\Delta[u_2]_{kl} = \sum_{k=i,l=j}^{k=n,l=m} \Delta[u_2]_{kl}, \qquad (18)$$

where the summation can be over any arbitrary path joining pixels (i, j) and (n, m).

The unwrapped displacement computed by (18) for a single push should be independent of the path chosen. This is rarely the case in practice due to errors in the differential displacement estimated in regions of small signal amplitude. The total displacement is wrong at **all** pixels using an unwrap

path passing through an erroneous point. This error is a serious problem with general unwrap algorithms. For displacement imaging, however, there are a large number of independent paths to any arbitrary pixel in the image plane from a stationary point. Therefore, independent estimates of the displacement can be obtained by summing along multiple paths. Obvious unwrapping errors can be removed through comparison of these independent estimates. Also, accumulated error in the total displacement can be reduced by averaging over all valid estimates.

We have used median filtering to both remove obvious unwrap errors and to reduce accumulated noise. For each pixel in the total displacement image, three independent paths are selected for unwrap. The first path unwraps along a horizontal line from (i, j) to (n, j) and then a vertical path from (n, j) to (n, m). The second path unwraps along a vertical line from (i, j) to (i, m) and then a horizontal path from (i, m) to (n, m). Finally, unwrap is performed along a diagonal path to reach either the mth line or the nth column. From this point either a simple horizontal or vertical line is used to complete the path to pixel (n, m). The median of these three independent estimates is used as the displacement measurement. Obviously, many more paths can be used to increase the dimension of the median filter. Results of experimental studies on tissue equivalent phantoms described in the next section, however, indicate that three independent unwrap paths per pixel are sufficient for accurate displacement images.

The unwrap procedure presented above can circumvent phase aliases for displacements greater than $\lambda/4$. For even larger displacements (on the order of 10λ) resulting in significant internal strain, however, all speckle tracking procedures break down if speckle features change as a result of the motion, as noted in Section I. To overcome this limitation, a large set of baseband images is recorded with small relative displacements comparable to a wavelength but with large total displacement from the beginning to the end of the set [15], [21]. Changes in speckle character between two neighboring images are small so that the displacement can be accurately estimated using (12)–(18). The total displacement over the set is computed by accumulating displacement measures between image pairs. This accumulation must be done carefully, however, since the initial condition for each image pair is continually changing. That is, the same speckle region must be tracked as it moves from image to image to produce the total displacement.

Formally, the total accumulated displacement $[u_2]_{nm}$ in a pixel (n, m) of the last image of the set is

$$[u_2]_{nm} = \sum_{i=1}^{I} [u_2]_{nj(i)}^i, \qquad (19)$$

where there are $I + 1$ images in the set with $i = 0$ corresponding to maximum surface displacement and $i = I$ corresponding to minimum surface displacement and $[u_2]_{nm}^i$ is the displacement between the $(i-1)^{\text{th}}$ and i^{th} images. Note that the vertical index in the accumulation must be adjusted from image to image such that

$$j(i) = j(i-1) + \left[\frac{[u_2]_{nj(i-1)}^{i-1}}{\Delta y} \right], \qquad (20)$$

where Δy is the vertical pixel spacing and $j(0) = m$. Obviously, $j(i)$ need not be an integer since v is a continuous function. To overcome this difficulty, we use simple linear interpolation to accumulate displacement measures from image to image. That is,

$$[u_2]_{nj(i)}^i = [1 - j(i) + j][u_2]_{nj}^i + [j(i) - j][u_2]_{nj+1}^i, \quad (21)$$

where j is the truncated integer representation of $j(i)$.

The vertical, longitudinal component of the second ranked strain tensor, or ε_{22}, is the spatial derivative of the vertical displacement with respect to vertical distance. That is, ε_{22} is

$$\varepsilon_{22} = \frac{\partial u_2}{\partial x_2} = \frac{\partial u_2}{\partial y}. \qquad (22)$$

Using a backward difference, discrete approximation for the derivative, the vertical strain can be computed directly from the accumulated displacement as

$$[\varepsilon_{22}]_{nm} = e_{nm} = \frac{[u_2]_{nm} - [u_2]_{nm-1}}{\Delta y}, \qquad (23)$$

where e_{nm} is ε_{22} at pixel (n, m). Although straightforward in concept, a strain image based on (23) often exhibits significant artifacts since small errors in the unwrap procedure at any given step i or from step to step are amplified by the derivative operator of (23). For example, if there is a large variance in the differential displacement at a particular image point, then the displacement at **all** pixels using an unwrap path through this point may be affected. Neighboring pixels not using an unwrap path including the aberrant point are unaffected. Spatial derivatives computed using these two types of pixels, therefore, may be subject to large error.

Large errors in the differential displacement at a particular point are often the result of small signal levels in the neighborhood of this point. From (17), the differential displacement is proportional to the phase difference between two neighboring pixels in the complex image $\tilde{z}$. A simple propagation of error analysis, therefore, yields the following expression for the variance of the strain computed according to (23) from a set of $I + 1$ base-band images:

$$
\begin{aligned}
\left[\sigma_\varepsilon^2\right]_{\text{direct}} &= \left[\frac{c}{2\omega_0 \Delta y}\right]^2 \sum_{i=1}^{I} \left[\frac{\sigma_0^2}{\left|\tilde{z}_{nm-1}^i\right|^2} + \frac{\sigma_0^2}{\left|\tilde{z}_{nm}^i\right|^2}\right], \\
&= \left[\frac{c}{2\omega_0 \Delta y}\right]^2 \left[\frac{I}{\text{SNR}_{nm}} + \frac{I}{\text{SNR}_{nm-1}}\right], \\
&= \left[\frac{c}{2\omega_0 \Delta y}\right]^2 \left[\frac{2I}{\text{SNR}_{nm}}\right],
\end{aligned}
$$

$$(24)$$

where σ_0^2 is the noise variance in image $\tilde{z}$, $\left|\tilde{z}_{nm}^i\right|^2$ is the signal power in the ith image at pixel (n, m), SNR_{nm} is the

average signal to noise ratio at pixel (n, m) over the set of I images and the last equation assumes that the signal to noise ratio of neighboring pixels is approximately equal. Clearly, if the signal to noise ratio is poor at any given pixel, then the variance is large. Since substantial spatial averaging was used to produce image $\tilde{z}$, zero signal magnitude is not expected. Nevertheless, small signals may still exist resulting in large fluctuations in the estimated strain.

To minimize the strain variance using (23), the estimated strain can be averaged using a 2-D spatial filter. Assuming a simple unity gain, moving average filter of dimension $K + 1$ by $K + 1$, the strain variance becomes:

$$[\sigma_\varepsilon^2]_{\text{direct}} = \left[\frac{c}{2\omega_0 \Delta y (K+1)^2}\right]^2 \sum_{k=n-\frac{K}{2}}^{k=n+\frac{K}{2}} \sum_{l=m-\frac{K}{2}}^{l=m+\frac{K}{2}} \left[\frac{2I}{\text{SNR}_{kl}}\right].$$

$$(25)$$

Again, if a single point has a very low signal to noise ratio, then any window including that point will have a large strain variance.

An alternative method relatively immune to unwrap artifacts directly computes a discrete estimate of the strain from a slightly modified version of (17). In this method, the differential strain between two consecutive images in the set of baseband images is computed from an estimate of the average **differential displacement between pixels** rather than from the average of the difference in unwrapped displacements between neighboring pixels. That is, the strain at pixel (n, m) is

$$e_{nm} = \frac{\Delta[u_2]_{nm}}{\Delta y} = \left[\frac{c}{2\omega_0 \Delta y}\right] \angle \text{LPF}\left[[\tilde{z}_{nm}][\tilde{z}_{nm-1}]^*\right],$$

$$(26)$$

where the complex product is filtered with a simple 2-D moving average filter **prior** to phase detection. Filtering of the complex signal, rather than of the phase itself, reduces strain variance for speckle objects, as shown below. Similar to the displacement, the differential strain of (26) computed from a pair of images must be accumulated over the complete set I. The final total strain e_{nm} is, therefore,

$$e_{nm} = \sum_{i=1}^{I} e_{nj(i)}^i,$$

$$(27)$$

where $j(i)$ is again given by (20). Note that unwrapping errors in the displacement do not destroy strain estimates since they only affect the pixel index $j(i)$. That is, unwrapping errors in any given subimage i leading to an erroneous $j(i)$ slightly misregister strain estimates from the same region. This error only tends to smear, or spatially low pass filter, strain images.

Assuming that the filter in (26) is a $(K + 1)$ by $(K + 1)$, 2-D moving average filter and that the signal to noise ratio of neighboring pixels is approximately equal, a propagation of error analysis yields the following expression for the variance in the strain estimated by the differential procedure of (26)
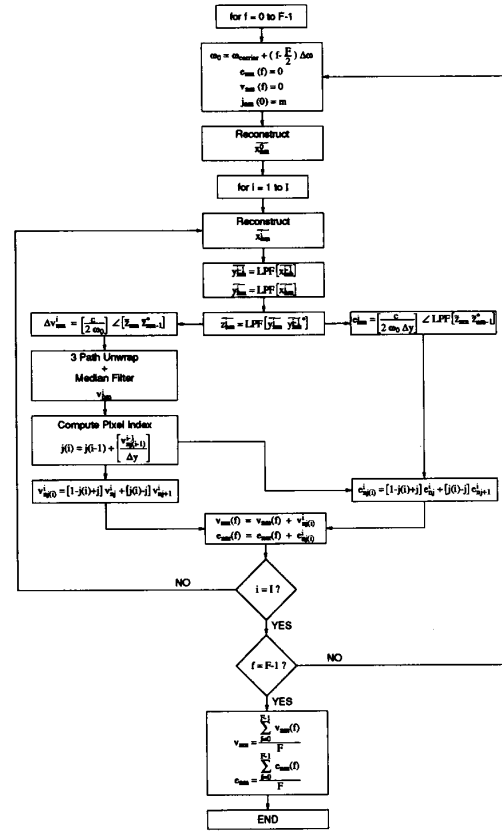

Fig. 5. Flow diagram of displacement and longitudinal strain computations.

and (27):

$$[\sigma_\varepsilon^2]_{\text{diff}} = \left[\frac{c}{2\omega_0 \Delta y}\right]^2 \left[\frac{2I}{\sum\limits_{k=n-\frac{K}{2}}^{k=n+\frac{K}{2}} \sum\limits_{l=m-\frac{K}{2}}^{l=m+\frac{K}{2}} \text{SNR}_{kl}}\right]. \quad (28)$$

In the limit where SNR is a constant over the filter window, (25) and (28) are identical. That is, if the signal level is constant over the filter window, then the differential method of (26) and (27) is equivalent to the direct method of (23). If signal levels vary over the filter window, however, then the differential method will **always** have a lower variance than the direct method. This difference is especially important for computing the strain in inhomogeneous materials, such as soft tissue, exhibiting a wide dynamic range in signal strength.

Finally, as noted in the discussion of (12), narrowband processing is used for phase sensitive speckle tracking over large displacements. Because broad-band transducers are employed for soft tissue imaging, there is the possibility of acquiring multiple, simultaneous, nearly independent estimates of tissue strain using different frequencies. In this paper, broad-band transducers are excited with an impulse. As part of the speckle tracking algorithm, however, the received

signal is demodulated to base-band and low pass filtered removing a significant fraction of the signal bandwidth. A simultaneous estimate of tissue motion is obtained by repeating the entire speckle tracking procedure using precisely the same transducer signals and filter bandwidths but with a shifted demodulator reference frequency. Since our demodulation scheme is entirely digital, multiple frequency processing is performed through slight alterations in a digital representation of the demodulator reference waveform. Simultaneous strain images resulting from this processing are simply averaged, as discussed in the next section. A flow diagram for the entire process is presented in Fig. 5.

IV. EXPERIMENTAL RESULTS

A 2-D schematic of our experimental system is illustrated in Fig. 4. The cylindrical axis of a gel-based phantom is placed perpendicular to the axis of a 128 channel, 1-D transducer array attached to the bottom of a water tank. The phantom is centered in the tank so that the image plane approximates the central axial plane of the phantom, where water provides contact between the array and phantom. Simple surface displacements are produced by a single, hydraulically driven block shaped piston 14 mm wide and 150 mm long located at the top of the phantom. Displacement of the piston, controlled by measuring arrival time differences to the central element of the array, produced deformation of the phantom as illustrated in Fig. 4. This setup closely approximates a 2-D mechanical system.

Experiments were performed on a number of gel-based phantoms, including a particular pair used for all results reported here. Two homogeneous cylindrical gels were made at the same time with nearly identical mechanical and ultrasonic scattering properties. Each 88 mm diameter by 140 mm long cylinder was constructed from 5.5% by weight gelatin and 0.4% by weight polystyrene microspheres (diameter of 40 to 120 μm) acting as ultrasonic scattering centers. A circular longitudinal hole 32 mm in diameter was made in the center of one phantom and filled with 12% by weight gelatin to simulate a hard inclusion. The ratio of the Young's modulus of the inclusion to that of surrounding material was estimated to be about 2.5 based on the approximately linear dependence of Young's modulus on gel concentration [29]. The scatterer concentration in the inclusion was the same as in the surrounding material making both phantoms nearly identical ultrasonically. Note that the inclusion could not be detected by manual palpation. Properties of these phantoms are discussed in more detail in [17].

Phantoms were imaged with a 82 mm wide, 1-D, 128 channel transducer array operating at 3.5 MHz. A synthetic aperture approach was used to reduce the amount of digital data needed to perform reconstructions. On a given firing, only two elements of the array were connected in parallel to a broad-band driver. The backscattered ultrasonic signal was detected by the same two elements connected in parallel to a broad-band pre-amplifier. The output of the pre-amp passed through a TGC amplifier and was digitized at a 14 MHz rate using a 12 bit analog to digital converter. These data


Fig. 6.   Conventional B-Scan image of one of the phantoms.

were stored for future processing. Under computer control of a 128 × 1 high voltage multiplexer, another firing was then initiated after the active pair of elements was electronically translated by one array position. This sequence continued until 127 radio frequency A-Scans were recorded for the 127 independent positions. Base-band images were reconstructed using a digital baseband demodulator with a simple constant f/number, synthetic aperture algorithm, where time delays were partitioned between physical delays and phase rotations of the base-band signal. By tying two elements together with a step size of only one element between firings, grating lobes of the synthetic aperture reconstruction were greatly reduced [30]. Measurements on wire targets indicate that this system has a lateral resolution of about 1 mm and an axial resolution of about 0.5 mm (full bandwidth) throughout the entire image plane.

In Fig. 6, the B-Scan image of one of the phantoms is presented. This image is 512 × 512 pixels distributed over a 100 mm × 100 mm square with the transducer array at the bottom and the piston at the top. The display is purely logarithmic over a 20 dB dynamic range. Clearly, the quality of B-Scans produced with this system is inferior to a traditional phased array scanner. Beam forming artifacts are evident at the boundaries of the phantom and in the vicinity of the piston. Nevertheless, images such as this are sufficient to test the displacement and strain methods presented above.

Quantitative estimates of the vertical component of the displacement ($[u_2]$) and the vertical longitudinal component of the strain tensor (ε_{22}) were reconstructed from a set of 21 images over a total vertical piston displacement of 4 mm with 200 μm steps between images. In addition, three simultaneous estimates of the displacement and strain were obtained at frequencies of 3.0, 3.5 and 4.0 MHz, where the ultrasonic bandwidth was restricted to 750 KHz for each frequency (i.e., the spectra partially overlapped). This filtering reduced the axial resolution to about 1 mm. Two-dimensional moving average filters with a spatial extent of 3 mm by 3 mm were used for all displacement and strain computations. Displacement images for the two phantoms described above are presented in Fig. 7, where Fig. 7(a) is the homogeneous phantom and Fig. 7(b) is the phantom with a hard inclusion. These images
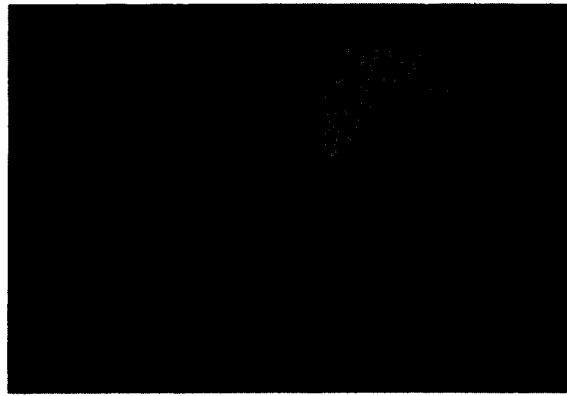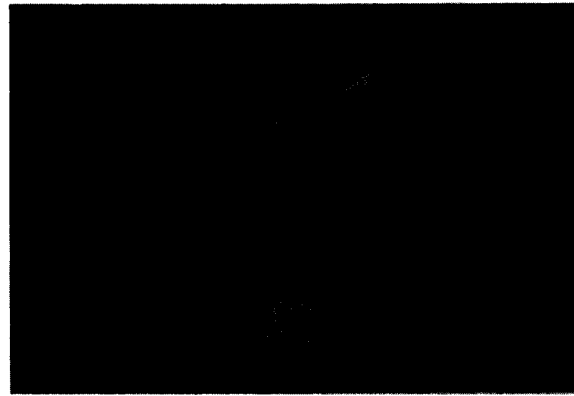
(a)
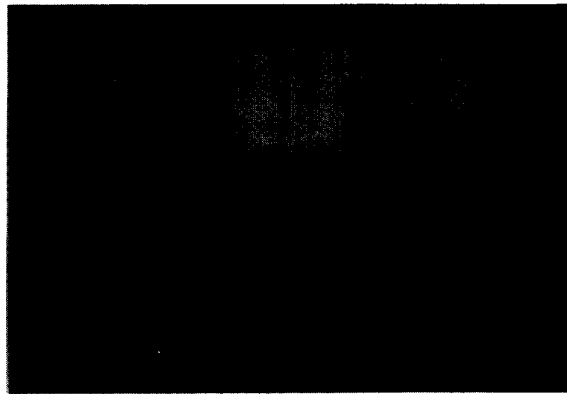
(b)

Fig. 7. Displacement images of two tissue equivalent phantoms using a quantitative gray scale with white representing a 4 mm vertical displacement and black representing no vertical displacement: (a) homogeneous phantom, (b) phantom with hard inclusion at the center.

(a)

(b)

Fig. 8. Quantitative images of the vertical, longitudinal component of the strain tensor. Both images are displayed over precisely the same dynamic range: (a) homogeneous phantom, (b) phantom with hard inclusion at the center.

are displayed over a linear, quantitative scale, where full brightness (i.e., white) represents a vertical displacement of 4 mm and complete darkness (i.e., black) signifies no vertical displacement. Clearly there are artifacts outside the boundaries of the phantom associated with imperfect beam forming. Within the phantom, however, the unwrapped displacement is a smooth function of position, where the central hard inclusion is slightly visible in Fig. 7(b).

Similar images of the strain are presented in Fig. 8, where Fig. 8(a) is the homogeneous phantom and Fig. 8(b) is the phantom with a hard inclusion. Both images are displayed over the same linear, quantitative scale, where full brightness represents a longitudinal strain of 5.4% and complete darkness represents a strain of 2.7%. The region of highest strain, starting at the top near the position of the piston and extending to the bottom near the transducer array, can be easily seen in both phantoms. In addition, the inclusion, representing a low strain region, is strikingly visible with position strongly correlating with the actual location of the inclusion. The signal to noise ratio of the strain image is a function of the magnitude of the strain. A representative value is estimated near the center of the homogeneous phantom where the strain approaches the

average value along the center line of about 4.5%. In this region, the signal to noise ratio (mean strain normalized to the standard deviation of the strain) is greater than 30. Similarly, the contrast to noise ratio, defined as the difference between the strain at the center of the inclusion and the strain at the same point in the homogeneous phantom normalized to the standard deviation of the strain, is greater than 15.

V. DISCUSSION

Images of soft tissue directly linked to the Young's modulus of linear elasticity may be possible if internal strain fields can be measured. In this paper we have shown that specific phase sensitive methods can be used to produce displacement and longitudinal strain images in the limit of large surface displacements. Phantom studies showed that surface displacements reaching 5% of the total object dimension, representing motion of about 10 ultrasonic wavelengths (20λ round-trip), can be used to generate strain images with signal to noise ratio greater than 30 and spatial resolution approaching 3 mm. With this level of contrast and spatial resolution, relatively small changes in Young's modulus may be readily detected.

Strain and displacement images were derived from low quality base-band images generated by a synthetic aperture system. As a result of the poor image quality, artifacts were present in both strain and displacement images, especially outside phantom boundaries. Similar to color masking used for real-time flow imaging systems, anechoic regions should be masked from final displacement and strain images based on B-Scan magnitude. In this study, however, image quality was too poor to permit proper masking of sidelobe artifacts outside the phantom. True clinical application of elasticity imaging will require a high quality imaging system to reduce displacement and strain artifacts due to improper beam forming. Nevertheless, the results presented in the previous section demonstrate the robustness of phase sensitive displacement and strain imaging methods even in the presence of extreme image artifact.

All measurements of motion were performed assuming that the object was in equilibrium (i.e., in a stationary position) after the application of a new surface displacement. Obviously, surface forces are not instantaneously transmitted to the interior of a mechanical body. That is, there is a finite travel time for these changes. To ensure equilibrium, images were not recorded until several seconds after the vertical piston was moved to a new position. Since 21 base-band images were obtained for each displacement and strain image, a complete experiment can last a few minutes. In most clinical situations such long data acquisition times are unacceptable because of the degree of intrinsic tissue movement relative to an ultrasonic wavelength over this period. That is, over a several minute data acquisition time internal structures may move by an ultrasonic wavelength due to cardiac motion, breathing and patient movement. Clearly, if strain imaging is to be clinically useful, then all data acquisition must occur at least within a patient breath hold (typically 2–3 s at minimum) so that only cardiac induced motion is present.

To acquire all data within a patient breath hold, each image of a 20–30 segment set may only take about 100 ms. Providing a small surface displacement on the order of several hundred μm in this period is not a problem. Propagation of this change throughout the body is limited by the low frequency shear wave velocity in tissue [31]. The zero frequency (DC) limit of the shear velocity in a viscoelastic medium such as tissue is simply

$$v_s = \sqrt{\frac{\mu}{\rho}}, \qquad (29)$$

where μ is the static shear elastic modulus (simply proportional to the Young's modulus in an incompressible material) and ρ is the density. Note that the shear wave velocity increases as a function of frequency so that the DC value represents the lower limit on wave speed. Using literature values for μ, the shear velocity at zero frequency in soft tissue ranges from about 1 m/s to 100 m/s [10], [29], [32]–[34]. This means that a small surface displacement can propagate between 200 mm and 4 m in 100 ms. Even given the possibility of shear wave reflections for non-DC components of the mechanical excitation, it appears surface displacements can propagate through soft tissue and reach equilibrium within 100 ms for most clinical imaging applications. Other slow time constant processes such as relaxation and creep should not influence motion on this time scale [35]. Future studies will be directed toward testing these hypotheses.

Although large scale motion can be minimized by recording all images over a single patient breath hold, cardiac induced motion will be present during data acquisition. To circumvent complications due to heart motion, base-band images of the object can be recorded at real-time rates with frame periods less than 30 ms. Thus over a 3 s data acquisition interval about 100 base-band images are recorded. This set of images can be used to monitor both propagation of the surface displacement throughout the tissue and cardiac induced motion. Using consecutive frames, large artifacts due to the heart can be identified and possibly reduced. Moreover, if an accurate model of cardiac motion can be constructed given the 100 base-band frames within an image set, then the effects of cardiac dynamics can be greatly reduced. This hypothesis will also be tested in future studies.

Images of tissue equivalent phantoms were obtained with surface displacements of about 5% of the total phantom dimension. Clinical palpation uses much larger relative surface displacements, often approaching 50% of tissue dimensions especially in the breast. At this level of deformation, internal motion cannot be described by linear elasticity theory. Nevertheless, detection sensitivity may be greatly enhanced using large surface deformations. The accuracy of strain imaging methods must be tested under these conditions to explore the ultimate sensitivity of the technique.

The spatial resolution for both displacement and strain images in this study is estimated to be between 3 and 5 mm based on a comparison of measured images to predictions of the theoretical model discussed in [17]. This resolution is limited primarily by the 3 mm extent of the spatial low pass filters used in displacement and strain computations. At this resolution, the measured strain has a signal to noise ratio of about 30. For spatial dimensions larger then the inherent resolution of the ultrasound imaging system, there is a direct tradeoff between spatial resolution in displacement and strain estimates and the signal to noise ratio. Thus, if strain estimates are computed to a spatial resolution comparable to the 1 mm resolving power of the ultrasound imaging system used in these studies, then both the signal to noise ratio and the contrast to noise ratio for the inclusion should be reduced by about a factor of 3–5. Consequently, images of the quality shown in this report may be possible at a resolution of about 1 mm if the inherent strain signal to noise ratio can be improved by about a factor of 3–5. Such gains are possible if larger total internal strains, smaller differential surface displacements, larger transducer bandwidths and higher quality ultrasound images are used to estimate the longitudinal strain. Future studies should be directed toward defining the ultimate limits on spatial and contrast resolution for strain imaging.

Only one component of the displacement vector and one component of the 2nd ranked strain tensor were measured. To fully characterize deformations of an elastic body, the complete strain tensor must be computed. Assuming a 2-D, incompressible (i.e., the sum of all longitudinal strains must

be zero) mechanical model of soft tissue, only one longitudinal and one shear component of the strain need be independently measured to fully represent the strain tensor. For a 2-D model, the symmetric shear strain is

$$\varepsilon_{12} = \varepsilon_{21} = \frac{1}{2}\left[\frac{\partial[u_1]}{\partial x_2} + \frac{\partial[u_2]}{\partial x_1}\right] = \frac{1}{2}\left[\frac{\partial[u_1]}{\partial y} + \frac{\partial[u_2]}{\partial x}\right],$$

(30)

where $[u_1]$ is the lateral component and $[u_2]$ is the vertical component of the displacement. To evaluate (30) the lateral, or cross beam, displacement must be estimated. Because of the anisotropy in spatial frequencies associated with diffraction limited ultrasonic imaging, estimation of cross-beam displacement is much less accurate than that of axial displacement [18]. Several techniques have been proposed for sensitive detection of lateral displacements, but even these methods will produce highly anisotropic errors in the two components of the shear strain defined in (30) [18], [22]. Consequently, studies of optimal methods for shear strain computation given the limits of diffraction limited ultrasonic imaging should also be undertaken.

If motion problems can be effectively eliminated using the procedures outlined above, then quantitative strain and displacement imaging have numerous potential clinical applications. Since palpation already is an active screening method for carcinomas of the breast, thyroid, testes and prostate, it is most probable that strain imaging can be directly applied to these pathologies. In particular, the ability to sense deep lying changes in Young's modulus as demonstrated in this study makes the method most attractive for breast cancer detection. Other possible applications are in nephrology and cardiology. Chronic nephritis, especially in transplanted kidneys, gives rise to significant scarring of the cortex prior to any functional changes [36]. Since scarring will presumably alter the Young's modulus of the cortex, early detection of chronic nephritis using quantitative strain imaging may be possible prior to the onset of significant functional problems. Similarly, changes in contractility are an early indicator of cardiac dysfunction. It may be possible to detect contractility alterations using quantitative strain methods such as those presented here [37]. Application of displacement and strain techniques on a microscopic scale using catheter based ultrasound may greatly assist coronary artery diagnosis and tissue engineering [22], [38]. Also, elasticity imaging may be used to monitor therapeutic procedures that greatly alter the mechanical characteristics of tissue, such as cryotherapy [39].

Finally, the quantitative accuracy of displacement and strain imaging must be established before such images can form the core of a reconstruction procedure aimed at quantitative Young's modulus imaging. In a companion paper, we explore the accuracy of our experimental results using a 2-D elastic model of the gel-based phantoms [17].

ACKNOWLEDGMENT

REFERENCES

[1] T. A. Krouskop, D. R. Dougherty and F. S. Levinson, "A pulsed Doppler ultrasonic system for making non-invasive measurements of the mechanical properties of soft tissue," *J. Rehab. Res. Dev.*, vol. 24, no. 2, pp. 1–8, 1987.

[2] R. M. Lerner, K. J. Parker, J. Holen, R. Gramiak, and R. C. Waag, "Sono-elasticity: Medical elasticity images derived from ultrasound signals in mechanically vibrated targets," *Acoust. Imaging*, vol. 16, pp. 317–327, 1988.

[3] M. Tristam, D. C. Barbosa, D. O. Cosgrove, J. C. Bamber, and C. R. Hill, "Application of Fourier analysis to clinical study of patterns of tissue motion," *Ultrasound in Med. & Biol.*, vol. 14, pp. 695–707, 1988.

[4] R. Adler, J. M. Rubin, P. Bland, and P. Carson, "Characterization of transmitted motion in fetal lung: Quantitative analysis," *Med. Phys.* , vol. 16, pp. 333–337, 1988.

[5] M. Bertrand, J. Meunier, M. Doucet, and G. Ferland, "Ultrasonic biomechanical strain gauge based on speckle tracking," *Proc. 1989 IEEE Ultrason. Symp.*, pp. 859–864, 1989.

[6] J. Meunier and M. Bertrand, "Ultrasonic speckle motion inherent to tissue motion: theory and simulation," *Proc. 1989 IEEE Ultrason. Symp.* pp. 865–868, 1989.

[7] J. Meunier *et al*, "Local myocardial deformation computed from speckle motion," *Computers in Cardiology*, pp. 133–136, 1989.

[8] A. P. Sarvazyan and A. R. Skovoroda, "New approaches in ultrasonic visualization of cancers and their quantitative mechanical characterization for differential diagnostics," *Abstracts of the All Union Conf. on Actual Problems of Cancer Ultrason. Diagnost.*, Moscow, November 9–11, 1990.

[9] R. M. Lerner, S. R. Huang, and K. J. Parker, "'Sonoelasticity' images derived from ultrasound signals in mechanically vibrated tissues," *Ultrasound Med. Biol.*, vol. 16, no. 3, pp. 231–239, 1990.

[10] Y. Yamakoshi, J. Sato, and T. Sato, "Ultrasonic imaging of internal vibration of soft tissue under forced vibration," *IEEE Trans. Ultrason. Ferroelect. Freq. Contr.*, vol. 37, pp. 45–53, 1990.

[11] A. P. Sarvazyan and A. R. Skovoroda, "Tissue characterization in medical imaging in terms of viscoelastic mechanical properties," *Abstracts of the 6th World Congress in Ultrasound*, Copenhagen, September 1–6, 1991.

[12] J. Ophir, I. Cespedes, H. Ponnekanti, Y. Yazdi and X. Li., "Elastography: a quantitative method for imaging the elasticity of biological tissues," *Ultrasonic Imag.*, vol. 13, pp. 111–134, 1991.

[13] F. Lee, J. P. Bronson, R. M. Lerner, K. J. Parker, S. R. Huang, and D. J. Roach, "Sonoelasticity imaging: results in *in vitro* tissue specimens," *Radiology*, vol. 181, pp. 237–239, 1991.

[14] A. P. Sarvazyan, A. R. Skovoroda, and D. Vucelic, "Utilization of surface acoustic waves and shear acoustic properties for imaging and tissue characterization," in *Acoustic Imaging*, H. Ermert, H. P. Harjes, Eds., vol. 19. New York: Plenum, 1992, pp. 463–467.

[15] S. Y. Yemelyanov, A. R. Skovoroda, M. A. Lubinski, B. M. Shapo, and M. O'Donnell, "Ultrasound elasticity imaging using Fourier based speckle tracking algorithm," *Proc. 1992 IEEE Ultrason. Symp.* , pp. 1065–1068, 1992.

[16] H. Ponnekanti, J. Ophir, and I. Cespedes, "Axial stress distributions between coaxial compressors in elastography: an analytic model," *Ultrasound in Med. & Biol.*, vol. 18, pp. 667–673, 1992.

[17] A. R. Skovoroda, S. Y. Emelianov, M. A. Lubinski, A. P. Sarvazyan, and M. O'Donnell, "Theoretical analysis and verification of ultrasound displacement and strain imaging," submitted for publication in the *IEEE Trans. Ultrason. Ferroelect. Frequency Contr.* , this issue, pp. 302–313.

[18] G. E. Trahey, J. W. Allison, and O. T. von Ramm, "Angle independent ultrasonic detection of blood flow," *IEEE Trans. Biomed. Eng.*, vol. BME-34, pp. 965–967, 1987.

[19] P. M. Embree and W. D. O'Brien, "The accurate ultrasonic measurement of the volume flow of blood by time domain correlation," *Proc. 1985 IEEE Ultrason. Symp.*, pp. 963–966, 1985.

[20] P. G. M. de Jong, *et al*, "Experimental evaluation of the correlation interpolation technique to measure regional tissue velocity," *Ultrason. Imaging* , vol. 13, pp. 145–161, 1991.

[21] E. J. Chen, W. K. Jenkins, and W. D. O'Brien, "The accuracy and precision of estimating tissue displacements from ultrasonic images," *Proc. 1992 IEEE Ultrason. Symp.*, pp. 1069–1072, 1992.

[22] M. O'Donnell, A. R. Skovoroda, and B. M. Shapo, "Measurement of arterial wall motion using Fourier based speckle tracking algorithms," *Proc. 1991 IEEE Ultrason. Symp.* , pp. 1101–1104, 1991.

[23] R. E. Boucher and J. C. Hassab, "Analysis of discrete implementation of generalized cross correlator," *IEEE Trans. Acoust., Speech and Signal Process.*, vol. ASSP-29, pp. 609–611, 1981.

[24] S. G. Foster, M. P. Embree, and W. D. O'Brien, "Flow velocity profile via time-domain correlation: error analysis and computer simulation," *IEEE Trans. Ultrason. Ferroelect. Freq. Contr.* , vol. 37, pp. 164–174, 1990.

[25] E. Weinstein and A. J. Weiss, "Fundamental limitations in passive time-delay estimation part II: wide-band systems," *IEEE Trans. Acoust., Speech and Signal Process.* , vol. ASSP-32, pp. 1064–1077, 1984.

[26] P. M. Embree, "The accurate measurement of the volume flow of blood by time delay correlation," Ph.D. Dissertation, Dept. Elec. Comput. Eng., Univ. Illlinois, Urbana-Champaign, 1986.

[27] D. L. Liu and M. Saito, "Restoring a δ-pulse train by spectral fitting," *IEEE Trans. Signal Process.*, vol. 40, pp. 2616–2619, 1992.

[28] M. O'Donnell and W. E. Engeler, "Correlation-based aberration correction in the presence of missing elements," *IEEE Trans. Ultrason. Ferroelect. Freq. Contr.*, vol. 39, pp. 700–707, 1992.

[29] A. P. Sarvazyan, "Low velocity of sound in gels and biological tissues," Ph.D. Dissertation, Pushchino, Instit. of Biophysics, USSR Acad. of Sciences, 1969.

[30] M. O'Donnell and L. J. Thomas, "Efficient synthetic aperture imaging from a circular aperture with possible application to catheter-based imaging," *IEEE Trans. Ultrason. Ferroelect. Freq. Contr.* , vol. 39, pp. 366–380, 1992.

[31] H. L. Oestreicher, "Field and impedance of an oscillating sphere in a viscoelastic medium with an application to biophysics," *J. Acoust. Soc. Amer.* , vol. 23, pp. 707–714, 1951.

[32] X. T. Troung, "Extensional wave-propagation characteristics in striated muscle," *J. Acoust. Soc. Amer.*, vol. 51, pp. 1352–1356, 1972.

[33] K. J. Parker, S. R. Huang, R. A. Musulin and R. M. Lerner, "Tissue response to mechanical vibrations for 'sonoelasticity imaging'," *Ultrasound in Med. & Biol.*, vol. 16, pp. 241–246, 1990.

[34] A. P. Sarvazyan, "Acoustic properties of tissues relevant to therapeutic applications," *Brit. J. Cancer*, vol. 45, supplement 5, pp. 52–54, 1992.

[35] R. H. Abbott and G. J. Steiger, "Temperature and amplitude dependence of tension transients in glycerinated skeletal and insect fibrillar muscle," *J. Physiol.*, vol. 266, pp. 13–42, 1977.

[36] G. Downer, S. Phan, and R. Wiggins, "Analysis of renal fibrosis in a rabbit model of crescentic nephritis," *J. Clinical Investigation*, vol. 82, pp. 998–1005, 1988.

[37] K. A. Wear and R. L. Popp, "Theoretical analysis of a technique for the characterization of myocardium contraction based upon temporal correlation of ultrasonic echoes," *IEEE Trans. Ultrason. Ferroelect. Freq. Contr.* , vol. UFFC-34, pp. 368–375, 1987.

[38] L. K. Ryan, G. R. Lockwood, B. G. Starkoski, D. W. Holdsworth, D. W. Rickey, M. Drangova, A. Fenster, and F. S. Foster, "A high frequency intravascular imaging system for investigation of vessel wall properties," *Proc. 1992 IEEE Ultrason. Symp.,* pp. 1101–1105, 1992.

[39] P. Laugier and G. Berger, "Experimental results of ultrasonic monitoring of cryotherapy on *in vitro* skin samples of domestic pig," *Proc. 1992 IEEE Ultrason. Symp.*, pp. 1045–1048, 1992.

Matthew O'Donnell (F'93), for a photograph and biography, see this issue, p. 313.

Andrei R. Skovoroda, for a photograph and biography, see this issue, p. 312.

Benjamin M. Shapo was born in Miami, FL, on March 8, 1964. He received the B.S.E. degree from Princeton University, Princeton, NJ, in 1986 and the M.S. degree from the University of Illinois at Urbana-Champaign in 1988, both in electrical engineering.

He is currently working towards the Ph.D. degree in the Biomedical Ultrasonics Laboratory at the University of Michigan. His research topic is intravascular imaging using catheter-based ultrasound transducer arrays.

Stanislav Y. Emelianov (M'94) for a photograph and biography, see this issue, p. 312.